

Article

Characterization of SPAD Array for Multifocal High-Content Screening Applications

Anthony Tsikouras ¹, Pietro Peronio ², Ivan Rech ², Nehad Hirmiz ³, M. Jamal Deen ⁴ and Qiyin Fang ^{1,3,*}

¹ Department of Engineering Physics, McMaster University, Hamilton, ON L8S 4L7, Canada; tsikoua@mcmaster.ca

² Dipartimento di Elettronica, Informazione e Bioingegneria, Politecnico di Milano; 20133 Milano, Italy; pietro.peronio@polimi.it (P.P.); ivan.rech@polimi.it (I.R.)

³ School of Biomedical Engineering, McMaster University, Hamilton, ON L8S 4L7, Canada; hirmizn@mcmaster.ca

⁴ Department of Electrical and Computer Engineering, McMaster University; Hamilton, ON L8S 4L7, Canada; jamal@mcmaster.ca

* Correspondence: qiyin.fang@mcmaster.ca; Tel.: +1-905-525-9140

Received: 26 September 2016; Accepted: 26 October 2016; Published: 31 October 2016

Abstract: Current instruments used to detect specific protein-protein interactions in live cells for applications in high-content screening (HCS) are limited by the time required to measure the lifetime. Here, a 32×1 single-photon avalanche diode (SPAD) array was explored as a detector for fluorescence lifetime imaging (FLIM) in HCS. Device parameters and characterization results were interpreted in the context of the application to determine if the SPAD array could satisfy the requirements of HCS-FLIM. Fluorescence lifetime measurements were performed using a known fluorescence standard; and the recovered fluorescence lifetime matched literature reported values. The design of a theoretical 32×32 SPAD array was also considered as a detector for a multi-point confocal scanning microscope.

Keywords: single-photon avalanche diode; time-correlated single-photon counting; confocal microscopy; time-resolved imaging; high-content screening; drug discovery

1. Introduction

In drug discovery, one of the most time-consuming stages is the identification of candidate drugs. Modern high-content screening (HCS) microscopes process thousands of living cell samples, which have been treated with varied dosages of drug leads. The resulting images are analyzed by advanced algorithms to determine the drug effectiveness and dosage optimization [1]. These results are analyzed for imaging phenotypes related to the cell's morphology and proliferation rate, as a means of determining the underlying reaction to the drug [2]. While important discoveries can be made through these phenotypes, it is impossible to determine the exact nature of how the drug is affecting the cell line.

Inside a cell, a complex interaction network of proteins exists to maintain homeostasis and regulate cell behavior [3]. Whether it is two proteins binding to each other or multiple proteins forming an oligomer, these protein-protein interactions happen at the scale of a few nanometers: far below the optical diffraction limit. Consequently, such interactions are invisible in morphological high-content screening. More insight can be obtained if a more direct approach to monitoring protein-protein interactions is used in HCS. Such techniques use existing information of these interactions, as well as their biological pathways, to enable a better understanding of how the drug works, as well as the side effects. One such directed approach is to use Förster resonance energy transfer (FRET), which offers the

ability to qualitatively and quantitatively monitor molecular interactions at nanometer scales. FRET is a phenomenon whereby an excited “donor” fluorophore non-radiatively transfers its excitation energy to a nearby “acceptor” fluorophore, which then fluoresces as it returns to the ground state. The proximity of the two fluorophores must be on the scale of <10 nm, which makes it suitable for tagging a specific protein-protein interaction [4]. While FRET can be monitored, to some degree, by measuring the ratio of donor emission to acceptor emission (“intensity FRET”), this method has complications, due to the differing local populations of donor and acceptor fluorophores and spectral bleeding effects between the excitation and emission spectra of the FRET pair [4,5]. Polarization-resolved FRET can be performed with a very good signal-to-noise ratio [6], but is complicated by losses and distortions due to polarization [7]. It also is not good at distinguishing between varying degrees of FRET [7].

Fluorescence lifetime imaging microscopy can measure FRET (FLIM-FRET), through monitoring the reduction in the fluorescence lifetime of the donor fluorophore. FLIM-FRET does not have the abovementioned complications, making it a more accurate measure of FRET activity—subsequently protein-protein interaction—within the cell. At the same time, fluorescence lifetime is also inherently more challenging to measure, however, since the targeted lifetimes are on the scale of 1–10 ns and the requirement of resolving the lifetime changes to a few hundreds of picoseconds. Furthermore, each pixel of an image could have many of the proteins of interest with differing degrees of FRET interaction. In the simplified case where both interacting and non-interacting fluorophores contribute to the same pixel, the fluorescence signal of the pixel would be a biexponential decay [8].

Time-correlated single-photon counting (TCSPC) is the gold standard by which FLIM is performed [9]. The principle is to measure the arrival times of each photon with very high precision, and form a histogram of arrival times as the fluorescence decay curve. This method requires the use of very low emission light levels in order to ensure that only a maximum of one photon arrives for each repetition, with the rule-of-thumb being a collection rate never exceeding 5% of the repetition rate [10]. Dividing the signal between multiple detectors and TCSPC circuits can proportionally improve the maximum allowable collection rate [11]. The method uses a raster scanning (confocal or multiphoton) approach, where each spot of the image is measured sequentially, with the signal being collected by a photomultiplier tube or single-photon avalanche diode (SPAD) [12]. Understandably, this makes TCSPC a challenge to apply to HCS, where a high priority is placed on acquisition throughput.

FLIM is also measured by time-gated imaging, where intensified charge-coupled device imagers (ICCDs) are made active for only a short time window [10,13]. By measuring multiple time windows over repeated excitations, an approximation of the fluorescence lifetime curve can be generated. Due to the large gate width (>300 ps), the ICCD gating is not able to achieve a suitably high time resolution in order to separate the components of biexponential decays. Typically, this technique only measures two time windows, and uses their ratio to measure an average fluorescence lifetime [13]. For a biexponential fluorescence decay, this is not ideal in determining the ratio of binding to non-binding FRET pair populations measured from a spot in the image. It is also a wide-field imaging technique, which not only affects the ability to resolve subcellular features, but also means that each decay represents a larger volume of the sample (including out-of-focus contributions), greatly reducing the precision of the FRET measurement [14]. Finally, it is a slow technique, due to the rejection of photons arriving outside of the time window, and the inherently low quantum efficiency of the image intensifier. FLIM can also be measured through frequency domain analysis. In its most common implementation, a modulated ICCD is used to collect phase and attenuation information at different frequencies [15], but this method suffers similar drawbacks as the time-domain gated-ICCD approach discussed previously.

While gated imaging and other analog approaches are faster and can be easier to implement, TCSPC is the most sensitive method of acquiring fluorescence decays, due to the discrete photon-counting nature that offers excellent signal-to-noise ratios [16]. This is especially important in the case of live cell imaging, where the number of available photons is severely limited because

low illumination intensities must be used since fluorophores are irreversibly photobleached after excitation [17].

In order to achieve a suitable effective spatial resolution and optical sectioning, confocal (or multiphoton) scanning fluorescence microscopy is required for measuring protein-protein interactions by FLIM-FRET [18]. While laser scanning can be performed very quickly and accurately, the time to acquire a confocal scan is limited by the collection time: the pixel dwell time must be set such that sufficient emitted light is collected at each spot in the image. While the laser power could be increased, in order to reduce the required dwell time, a very high laser irradiance could lead to photobleaching and photodamage of the specimen. Furthermore, if time-resolved data is being collected by TCSPC, the emitted photon collection rate must be kept below 5% of the laser repetition rate in order to prevent pulse pileup distortions in the fluorescence decay curve. This further limits the maximum laser power that could be used for sample illumination.

As an example, a 256×256 FLIM image, requiring 10,000 counts per pixel for suitable biexponential fitting, would then need 655×10^6 photon counts. At a 40 MHz repetition rate—the repetition rate best matched for the range of biological fluorescence lifetimes—the highest collection rate would be 2 Mcps (5% of 40 MHz). Therefore, the image would take nearly 330 s to acquire. The goal for high-throughput screening, however, is typically benchmarked to be 100,000 assays per day, or one acquisition per second [19].

If the speed of confocal imaging cannot be improved by increasing the excitation energy, the alternative would be to parallelize the confocal process. By employing multiple foci to scan across the sample, the laser power for each focal spot could be kept low to protect against photodamage and remain TCSPC-friendly, but the combined excitation at the sample plane can be much higher. The imaging speed of a system like this would then scale with the number of excitation foci. An additional benefit to using lower laser powers is that a single sample can be imaged repeatedly without photobleaching. This allows for the creation of a timelapse sequence capturing the dynamics of protein-protein interactions.

The main challenge of achieving multiplexed FLIM has been in the lack of a suitable detection module capable of sub-nanosecond response as well as digitization of such fast signals. Photomultiplier tubes (PMT) are the most commonly used detectors for single-photon counters, but they are generally too large and expensive to implement in a large parallel detection scheme [20]. PMTs typically have an active area diameter of 8 mm or larger and further miniaturization is limited since a great deal of their assembly is done manually.

The largest commercially available multi-anode PMT that has been implemented for TCSPC has 16 channels and a total active area of $16 \times 16 \text{ mm}^2$ (Becker and Hickl PML-16, Berlin, Germany). In this instrument, count signals from the 16 anodes are routed to eight TCSPC channels. Another research group [21] has been developing microchannel plate (MCP) PMTs with a multi-anode readout of 32×32 pixels, though this is still under development. MCP PMTs have the advantage that they are already greatly multiplexed due to their pore structure, and their low transit time spread gives them the best temporal resolution among TCSPC detectors. However, interfacing between the anodes and the TCSPC electronics has proven difficult. Recently, a wide-field approach to TCSPC was developed using an MCP PMT with a crossed delay line anode detector for spatially resolving each photon count [22]. This technique has the benefit of making TCSPC achievable in non-scanning setups, making it suitable for techniques such as light-sheet microscopy and total internal reflection microscopy. However, it can only achieve the collection rate of a single PMT. Since it is not actually a multiplexed solution, there is no gain in throughput and it is not a solution for HCS.

The possibility of multiplexing is now feasible with the advent of solid-state detector arrays specially designed for time-resolved imaging. There are a number of research groups actively pursuing integrated circuit detector arrays that are capable of creating hundreds to thousands of independent time-resolved pixels. A large number of these efforts involve the use of SPAD arrays using TCSPC [23–26], while there are a few on-board time-gating approaches [27–29].

In addition to the clear advantages of size and scalability, SPADs match or outperform PMTs in other aspects. Their time resolution, usually determined by the transit time spread of a detected photon, is on the scale of 50 ps, compared to 100 ps or longer in conventional PMTs [19,20]. However, MCP PMTs are indeed capable of a shorter transit time spread [30]. Silicon-based SPADs are also more efficient and well-tuned to the emission range of biological fluorophores: such SPADs have a quantum efficiency of nearly 50% at 500 nm, while it is less than 20% for a PMT [31,32]. Hybrid PMT-SPAD detectors with a GaAsP photocathode are capable of 50% peak quantum efficiency as well, though these are costly and have not yet been developed into an array [33]. Possibly the most significant benefit to a SPAD array is low cost, as integrated circuits are significantly cheaper to manufacture than vacuum-tube technology.

We have previously designed a multiplexed confocal setup [34,35], which uses a microlens array to generate a grid of foci. A galvo-mounted window is used to raster scan the foci across the sample, and then de-scan the returning emission light back in line with the microlenses. The returning light that transmits through the dichroic filter is collimated, but spatially encoded by the different lenslet channels. A single pinhole is used to achieve confocality for all of the channels, before the light is collimated once more, then separated into foci by a second microlens array. The end result is that we have a multifocal confocal setup in which the emission foci at the detector plane remain stationary. This means that discrete stationary detectors can be used to collect the signals, unlike spinning disk confocal setups where the emission foci are painted across an imaging sensor.

By placing a SPAD array at the detector plane, it would be possible to create a high-speed confocal imager with very high temporal resolution. Since the TCSPC process is multiplexed, the acquisition time would no longer be limited to prevent pulse pile-up distortions. In this project, we explored the possibility of implementing a custom-made SPAD array with an integrated TCSPC chip for HCS FLIM. Based on the performance of a 32×1 channel SPAD array, we determine that the future development of a 32×32 channel array would be suitable for achieving high-speed FLIM.

2. Materials and Methods

2.1. Requirements for FLIM

It is difficult to state the de facto requirements for FLIM, since it can be very dependent on the particular sample, selection of fluorophore, and feature of interest. For instance, if the fluorescence lifetime quenching is significant enough, then an average lifetime measure could be sufficient to determine the FRET efficiency. Similarly, if the features of interest in the sample are relatively large, TCSPC histograms from each pixel of the feature can be binned together, meaning that fewer counts are required per pixel in order to get a good fit. Finally, the required field-of-view and spatial resolution also depend on the sample of interest.

For the sake of comparison, we will narrow the discussion to a typical case, where a $100\times$ immersion objective is used. The pitch between foci in our experimental setup is $400 \mu\text{m}$. With a 32×32 array of foci, the field of view at the microscope input is $12.8 \times 12.8 \text{ mm}$ —roughly the input aperture limit of commercial microscope side ports. After the $100\times$ objective, this translates to a $128 \times 128 \mu\text{m}$ field-of-view at the sample, with a foci pitch of $4 \mu\text{m}$. To achieve $0.5 \mu\text{m}$ resolution, a 16×16 raster scan is required, meaning 256 scan acquisitions are needed to collect the entire FLIM image—which would have a pixel resolution of 512×512 .

Since each SPAD would be responsible for collecting a 16×16 subset of this image, it would need to collect each TCSPC histogram in 3.9 ms. If approximately 10,000 counts are required in order to fit a biexponential decay, then each SPAD should be capable of collecting at least 10,000 counts at each scan position, which works out to 2.56 Mcps.

The required temporal resolution is also specific to the experiment, and depends on both the fluorescence lifetime range of the fluorophores present, and the impulse response function (IRF) of the excitation source. For ultrashort laser pulses, such as a Ti:sapphire laser, the laser pulse can be

considered an ideal impulse, and so its pulse shape will not impact the fluorescence decay. In the case of diode lasers, whose full-width half-maximum pulse width is on the order of 100 ps, this ideal impulse assumption is no longer valid, and the IRF is required in order to deconvolve and properly fit the collected decay. It is then required that the temporal resolution of the TCSPC signal be sufficient to resolve the IRF. This can be accomplished with 25 ps time bins.

Given a repetition rate of 40 MHz, and thus a period of 25 ns, this means that 1000 time bins are required to collect the histogram. While the target number of counts per histogram is 10,000, it is unlikely that the peak number of counts per bin will exceed 1000, and so a 10-bit dynamic range would be sufficient.

The data transfer rate is a final concern with regards to the SPAD array solution. Based on the above calculation, a single histogram would be 10,000 bits in size. Since each SPAD would be transferring 256 histograms per second, then the data transfer rate for a single SPAD would be 2.56 Mbps. The entire 32×32 SPAD array would then have a transfer rate of 2.62 Gbps. This is comfortably possible with current generation readout speeds, such as USB 3.0, which can transfer data at a speed of 5 Gbps.

2.2. SPAD Array Characteristics

A customized SPAD array was used in these experiments. Its architecture and performance characterization have been previously reported in detail [26]. It has 32 one-dimensional pixels, which are 50 μm in diameter and spaced at 250 μm from each other. A summary of the SPAD array specifications can be found in Table 1. The SPAD chip has a USB output to read photon counting data from all 32 channels. It also connects to a customized TCSPC box consisting of four eight-channel time-to-amplitude converters (TAC) [26]. TCSPC histograms are compiled on-chip, and can be read out in real-time via another USB connection. Characterization experiments were performed previously on the SPAD array prototype. Results of the characterization are collected in Table 1.

Table 1. Characteristics of the 32-channel SPAD array.

Type	Characteristics		Ref.
Pixel Size	50 μm		
Pixel-to-Pixel Pitch	250 μm		
Array Size	32×1		
Pixel Output Dead Time	16 ns (min)		
TAC Dead Time	250 ns		
Photon Detection Efficiency	45% @ 540 nm (peak)		[26]
	25% @ 700 nm		
	$-10\text{ }^\circ\text{C}$	$25\text{ }^\circ\text{C}$	[26]
Dark Count Rate (per Pixel)	<600 cps (90%)	<10 kcps (90%)	[26]
	4 kcps (max)	60 kcps (max)	
Temporal Resolution	65 ps		[26]
Afterpulsing Probability ($-10\text{ }^\circ\text{C}$)	<1.6% (90%)		[36]
	1.9% (max)		
Optical Crosstalk	1.8% (adjacent)		[36]
	0.07% (two away)		
	negligible (further)		

Many SPAD arrays are being developed using standard CMOS processes, since this allows for monolithic integration of electronics alongside the SPAD detectors, and cheaper fabrication. CMOS processes, however, have a number of limitations that are not ideal for SPAD development, including shallow implant depths, low doping concentrations, and design rule restrictions [37,38]. This SPAD array is unique from most other emerging options because it is not made with a standard CMOS

process. The customized process is more costly to fabricate, but allows greater control over their characteristics so as to achieve higher temporal resolution and better quantum efficiency.

It also presents challenges in scaling up the array. While the SPADs are fabricated via a custom process, the detection electronics are standard CMOS. What this means is that the SPAD array cannot be constructed as “smart pixels”, in which each detector’s electronics is designed to fit in the interstitial space between SPADs. Instead, the TACs are not on the same chip, and are only interfaced with the SPAD array along the perimeter. For larger SPAD arrays using this interfacing method, it becomes difficult to provide a dedicated TAC for every SPAD. Furthermore, the custom-designed SPADs and TACs are very power intensive (40 W for 32 SPADs, and 30 W for 32 TCSPC channels [26]), requiring large power supplies and heat dissipation techniques.

SPADs are able to generate an avalanche effect, where the signal for a single photon is amplified to produce a macroscopic signal. The arrival of an emitted photon results in a quickly rising current that reaches a steady-state signal in less than a nanosecond. More importantly, the jitter of this rising edge is typically in the range of picoseconds. TCSPC works by accurately discriminating the time of this rising edge relative to the excitation pulse, therefore measuring the arrival time of the photon. After many repeated trials, it is possible to generate a histogram of emitted photon arrival times, which can be fit as a fluorescence decay.

There are many important parameters involved in characterizing SPADs for photon-counting. First, the photon detection efficiency (PDE) of the detector dictates the likelihood that a photon incident on the detector will be counted. Higher efficiency is always beneficial, since this either means that the TCSPC histograms can be accumulated in a shorter time, or that a lower laser power can be used, which is less likely to damage or photobleach the sample. The uniformity of the PDE in the array is also a concern. Since the scan is done with all foci in parallel, the scan rate is limited by that of the SPAD with the worst PDE. SPADs also have an upper bound collection rate due to the 5% TCSPC limit, so increasing the laser power to accommodate the worst performing SPAD may push the best performing SPAD into a pulse pile-up situation. The PDE was previously measured using an integrating sphere and monochromator to generate uniform quantifiable light [26]. The SPADs were measured to have a peak PDE of approximately 45% at 540 nm, and a relatively slow fall-off towards longer wavelengths, still achieving 25% PDE at 700 nm.

There are actually multiple possible sources of pulse pileup distortion, beyond the 5% TCSPC limit discussed here. First, the SPAD itself has a dead time after each count, where it cannot receive another count. The dead time in this case is 20 ns, meaning it is unlikely to be a factor when compared to the 5% TCSPC limit. In other words, the 5% TCSPC limit already ensures that two photons do not arrive within the same 25 ns period, so it follows that they also would not arrive within 20 ns of each other. The TAC also has a dead time of 250 ns after each count, which could be a minor source of lost counts, but is unlikely to cause any skew to the resulting histograms [11].

Another parameter of interest is dark count rate (DCR). A dark count in this case is when an electron spontaneously sets off an avalanche effect which is not related to the arrival of a photon. Similar to dark current in an image sensor, the DCR increases with operating temperature. SPADs often vary widely in terms of their characteristic DCR, and the highest DCR would limit the speed at which the image can be acquired with a suitable signal-to-noise ratio. The DCR was previously found by measuring collection rates for each SPAD while the detector was in a dark environment [26]. At room temperature, the DCRs of the SPADs ranged from 200 cps to 60 kcps. The highest DCR is not very representative of the overall DCR distribution, as 90% of the SPADs had a DCR of less than 20 kcps. When measured at $-10\text{ }^{\circ}\text{C}$, the range of DCR values is from 15 cps to 4000 cps, with 90% of SPADs featuring a DCR less than 600 cps. There does not appear to be any pattern as to where the high DCR SPADs are situated on the chip, and so the variability in DCR is more likely to be associated with variability in the manufacturing process of each individual SPAD than with device geometry considerations.

Afterpulsing has a unique mechanism for SPADs [39]. This is when a charge from a previous avalanche gets trapped in a material defect, and starts its own avalanche at a later time. The likelihood of this occurring is known as the afterpulsing probability (AP). The result is very similar to dark counts, except the number of erroneous counts are proportional to the collection rate. Afterpulsing is different in PMTs, since it results in a set of afterpulses at discrete time delays from the original pulse, where the time delays correspond to different ionized residual gases in the vacuum tube [40,41]. By comparison, SPAD afterpulsing is much more uniform across the histogram and, therefore, can be removed as a uniform background subtraction [42]. Afterpulsing can be minimized by applying a longer hold-off time for the SPAD, but this comes at the cost of a reduced repetition rate for the experiment. It can also be reduced by increasing the temperature of the SPAD array, since this will reduce the lifetime of the trapping sites. Increasing the temperature, however, will also increase the DCR. The afterpulsing that remains after a hold-off period is also expected to be very long-lived, and not very sensitive to changes in temperature or longer hold-off times. The afterpulsing probability (AP) was previously measured using the time-correlated carrier counting technique and is found to be less than 1.9% across the entire SPAD array when measured at $-10\text{ }^{\circ}\text{C}$ [36].

In addition to detector-specific noise sources, a major source of uncertainty in a TCSPC histogram is shot noise due to the stochastic nature of photon counts. The dark counts and afterpulsing counts might skew the histogram towards longer decays, but this can be corrected by subtracting off the noise background. What is left once this is done is the added uncertainty in the number of counts in each bin due to these noise sources. Since shot noise is unavoidable, the goal of a good avalanche detector would be to keep extrinsic noise sources low enough that the shot noise remains the dominant source of noise in the measurements.

Optical crosstalk refers to when a light signal incident on one SPAD results in counts on adjacent SPADs. When a photon triggers an avalanche, secondary photons are emitted from the SPAD which can trigger other avalanches in nearby SPADs. This crosstalk can be caused by either direct optical paths between detectors, or light reflecting off the bottom of the chip [43]. The measure of optical crosstalk is a percentage, referring to what fraction of photon counts at the original SPAD are also measured at a secondary SPAD. The crosstalk can be measured with respect to adjacent SPADs or further removed SPADs, and diminishes quickly with distance. Optical crosstalk from a bright feature could result in artifacts appearing in the reconstructed images of adjacent SPADs. Optical crosstalk was measured between adjacent and non-adjacent SPADs, and was measured to be 1.8% for adjacent SPADs (250 μm separation), and 0.07% for next-to-adjacent SPADs (500 μm separation) [36]. SPADs at further separations resulted in negligible crosstalk.

The temporal resolution of a SPAD depends on transit time spread at the detector and the timing accuracy of the TCSPC electronics. This can be as low as tens of picoseconds. The resolution is not the whole story: the linearity of the time axis is also important in order to ensure that the collected fluorescence signal is not distorted. The time resolution was measured using a fiber laser with sub-picosecond FWHM, and was determined to be 65 ps under typical collection rates, with excellent differential non-linearity performance [26].

As discussed in the introduction, the TCSPC readout sets a limit on the allowable collection rate of 5% of the repetition rate: for a 40 MHz repetition rate, the collection rate must be kept below 2 MHz. In addition to this, the TAC has its own bandwidth limitation of 4 MHz. Therefore, in a typical one SPAD to one TAC arrangement, the collection rate is still TCSPC-limited.

Finally, when greatly multiplexing the acquisition process, the sheer size of the data readout becomes a concern. The imaging rate is ultimately limited by how quickly the data can be read out at each scan position. This depends on the data transfer protocol as well as the data size of each histogram.

2.3. Experimental Methods

Fluorescence lifetime experiments were performed using the experimental setup is shown in Figure 1. The SPAD array was tested by measuring the fluorescence lifetime of Coumarin 6 using

a 470 nm diode laser head (PicoQuant LDH-P-C-470, Berlin, Germany). The laser was directed towards a cuvette of Coumarin 6, and the fluorescence was collected along a perpendicular path by a pair of lenses. After passing through an emission filter (Semrock FF542/27, Rochester, NY, USA), the fluorescent light was then focused onto the SPAD array, and the positioning was adjusted in order to attain a roughly uniform collection rate of 1 Mcps across the 32 detectors. The acquisition was done at a 40 MHz repetition rate, and an acquisition time designed to achieve differing total numbers of counts. Four conditions were tested: 1000 counts, 5000 counts, 10,000 counts, and a large number of counts (20,000,000), to see the impact on lifetime estimation.

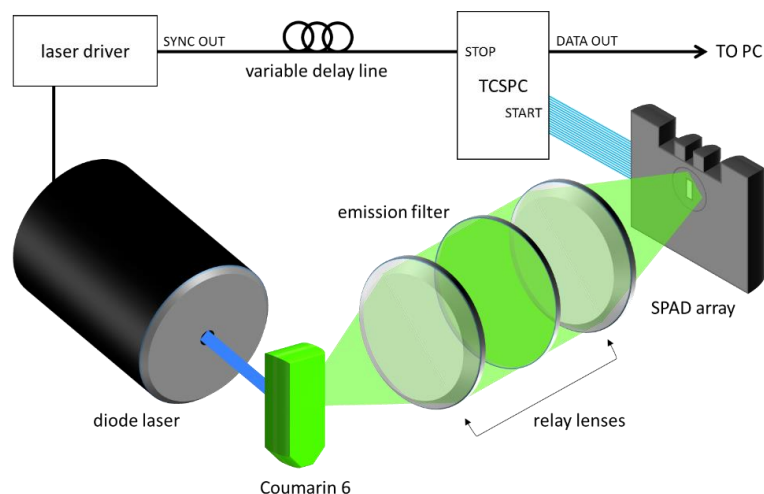


Figure 1. Experimental setup. Pulsed laser light is used to excite and fluoresce a cuvette of Coumarin 6 dye. The signal is collected perpendicular to the excitation using a pair of relay lenses and an emission filter, and focused onto the SPAD array. The laser driver is synchronized with the TCSPC through a variable delay line.

3. Results

3.1. Photon Detection Efficiency (PDE)

As the majority of fluorophores of interest have emission peaks in the 500–600 nm range, the 540 nm peak of the SPAD detector and slow roll-off towards longer wavelengths is an ideal fit.

There also appears to be great uniformity with regard to PDE across the SPAD array. At 500 nm, the PDE across all 32 channels ranges from 42% to 44%. It is worth noting that, for the application of multiplexed confocal FLIM, the SPAD with the lowest PDE can be limiting to the system. In order to achieve sufficiently high image quality across the entire region of interest, it is important that each detector is able to obtain sufficient counts. In the case where there is a high variability in PDE, the scanning process needs to be slowed down such that the SPAD with the lowest PDE can achieve a sufficient SNR. The laser power of the setup could be increased instead, but the maximum collection rate of the SPAD with the highest PDE must still be kept below 5% TCSPC limit. Fortunately, with a PDE that varies by $\pm 2.5\%$, PDE non-uniformity is not a significant issue.

3.2. Dark Count Rate (DCR)

Similar to the case of PDE, the noisiest SPAD can be severely limiting to the system. Since all of the SPADs acquire signal for the same time period, the entire scan can be slowed down by the SPAD with the highest noise in order to maintain a suitable SNR. Given that the maximum count rate is TCSPC-limited to 2 Mcps, and assuming that the pixels in the image will have a contrast ratio of at least 100:1, it is implied that there will be foci on the sample where collection rates of 20 kcps or less are expected. In these cases, it becomes quite problematic when the signal is of the same

magnitude as the noise. Fortunately, the SPAD array is capable of being cooled to $-10\text{ }^{\circ}\text{C}$. This has been tested previously in Milan, and found to reduce the largest DCR by an order of magnitude, from 60 kcps to 4 kcps [26]. The variability of SPAD DCR performance remains a concern, but appears to be manageable under cooled conditions. The relation between noisy channels and the presence of impurities is under investigation.

3.3. Afterpulsing Probability

A maximum afterpulsing probability of 1.9% implies that a 2 Mcps SPAD would be accompanied by less than 40 kcps of spurious counts associated with afterpulsing. Afterpulsing counts cannot be directly compared to dark counts, though. Since afterpulsing counts and acquired signal both scale with the collection rate, afterpulsing is never able to dominate the signal. In contrast, while a high-level signal can effectively eliminate the impact of dark counts, afterpulsing counts scale with the signal, and so are indicative of the highest achievable SNR of the detector.

3.4. Comparison to Shot Noise

As mentioned earlier, an ideal TCSPC detector would be one in which its own noise sources are not significant when compared to the shot noise of the TCSPC process. It is then important to define equations for shot noise as well as the DCR and AP noise. The signal dS associated with a single exponential decay can be described as:

$$dS = \frac{N}{\tau} \exp\left(-\frac{t}{\tau}\right) dt \quad (1)$$

where N is the number of photon counts, τ is the fluorescence lifetime, and t is the histogram time. The number of photons arriving within a time window can be found by integrating the function between the time window bounds, t_1 and t_2 . The shot noise n_s is the square root of the number of counts in a time window, and so can be expressed as:

$$n_s = \sqrt{\int_{t_1}^{t_2} dS} = \sqrt{\frac{c T}{\tau} \int_{t_1}^{t_2} \exp\left(-\frac{t}{\tau}\right) dt} \quad (2)$$

where N has been replaced by the product of the collection rate c and the integration time T . The dark signal dD would have a uniform distribution with respect to time. This signal can be described as:

$$dD = \frac{(\text{DCR}) T}{P} dt \quad (3)$$

where DCR is the dark count rate and P is the period. Similarly, the number of dark counts in a time window can be found by integrating over the time bounds, and the dark noise n_D will be the square root of this value:

$$n_D = \sqrt{\int_{t_1}^{t_2} dD} = \sqrt{\frac{(\text{DCR}) T}{P} \int_{t_1}^{t_2} dt} \quad (4)$$

Afterpulsing signal dA can be approximated as a uniform distribution in this case as well. The signal is defined as:

$$dA = \frac{(\text{AP}) c T}{P} dt \quad (5)$$

where AP is the afterpulsing probability. Once more integrating over a time window and taking the square root gives the expression for afterpulsing noise n_A :

$$n_A = \sqrt{\int_{t_1}^{t_2} dA} = \sqrt{\frac{(\text{AP}) c T}{P} \int_{t_1}^{t_2} dt} \quad (6)$$

Using Equations (2), (4), and (6), an expression for the ratio of total noise n_T to shot noise n_s alone can be solved:

$$\frac{n_T}{n_s} = \frac{\sqrt{n_s^2 + n_D^2 + n_A^2}}{n_s} \tag{7}$$

This is solved and simplified to yield:

$$\frac{n_T}{n_s} = \sqrt{1 + \frac{\tau}{P} \left(\frac{(\text{DCR})}{c} + (\text{AP}) \right) \exp\left(\frac{t}{\tau}\right)} \tag{8}$$

Equation (8) presents how much larger the uncertainty is once the device-specific noise sources are included. Using the measured values for DCR and AP, it is possible to determine how significant of a contribution these mechanisms will have on the resulting histograms. As an example, we consider a target fluorophore with a lifetime of 5 ns. The added noise is calculated over a time window of twice the fluorescence lifetime, and for a range of collection rates from 10 kcps to 2 Mcps. The DCR of the worst performing SPAD is used for the cooled ($-10\text{ }^\circ\text{C}$) and room temperature ($25\text{ }^\circ\text{C}$) cases, while the afterpulsing rate of 1.9% is used. Contour plots according to Equation (8) are generated for these ranges of parameters in Figure 2.

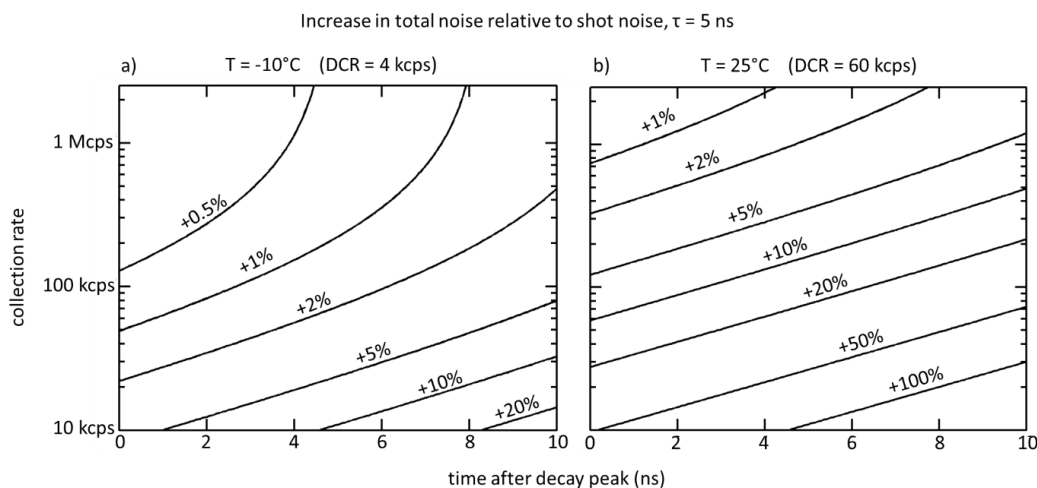


Figure 2. Increase in total noise along TCSPC histogram compared to shot noise alone for a 5 ns fluorescence decay at (a) $T = -10\text{ }^\circ\text{C}$ and (b) $T = 25\text{ }^\circ\text{C}$. Contour lines indicate the increase in total noise in terms of percentage of the shot noise.

3.5. Optical Crosstalk

In the context of the multiplexed confocal microscope, optical crosstalk represents another type of signal contamination. There is still a time-correlated nature to it, and so the time-resolved signal from one channel can spread into an adjacent channel, adding its own lifetime components, as well as its intensity. While a 2% contribution of crosstalk may not be very significant when adjacent SPADs are receiving photons at roughly the same collection rates, it can be quite problematic when a SPAD is measuring low-level signals while adjacent SPADs are measuring high signals. In other words, this affects the maximum contrast ratio that can be obtained in a reconstructed image. This would also be a more critical issue in a 2D SPAD arrangement, when each SPAD has eight adjacent SPADs that can contribute to crosstalk.

It is worth noting that the optical crosstalk of this 32-channel SPAD array was an order of magnitude higher than the crosstalk value measured in the Milan group’s eight-channel SPAD array (0.2%). It is suspected that the cause of the increased crosstalk is due to a change in device substrate.

If the crosstalk can be reduced to these previously attained levels, then it should not cause significant intensity or temporal artifacts in a reconstructed FLIM image.

3.6. Temporal Resolution

With the current design, the TCSPC histogram is divided into 2^{14} columns, meaning that the temporal bin size for a 25 ns full scale range is 1.5 ps. This is far below the temporal resolution of the SPAD array, adding nothing to the actual resolution while requiring more data to be transferred.

3.7. Lifetime Estimation

The standard log-linear fit method was employed. First the TCSPC histograms were temporally binned to have a 50 ps bin size. An example of this is shown in Figure 3a. Next, the flat noise level was subtracted from each histogram. The histograms were then truncated to start at the peak of the decay. The logarithm was taken of each histogram, such that a single exponential decay becomes a first-order polynomial, and the negative inverse of its slope is the fluorescence lifetime. Finally, a linear least squares fit was performed, but this fitting was truncated to end at the first bin with zero counts. The resulting lifetime fits for one of the SPADs are shown in Figure 3b. The average lifetime estimated under each count condition are shown in Figure 3c, with 95% confidence interval bounds associated with all of the SPADs' individual measurements.

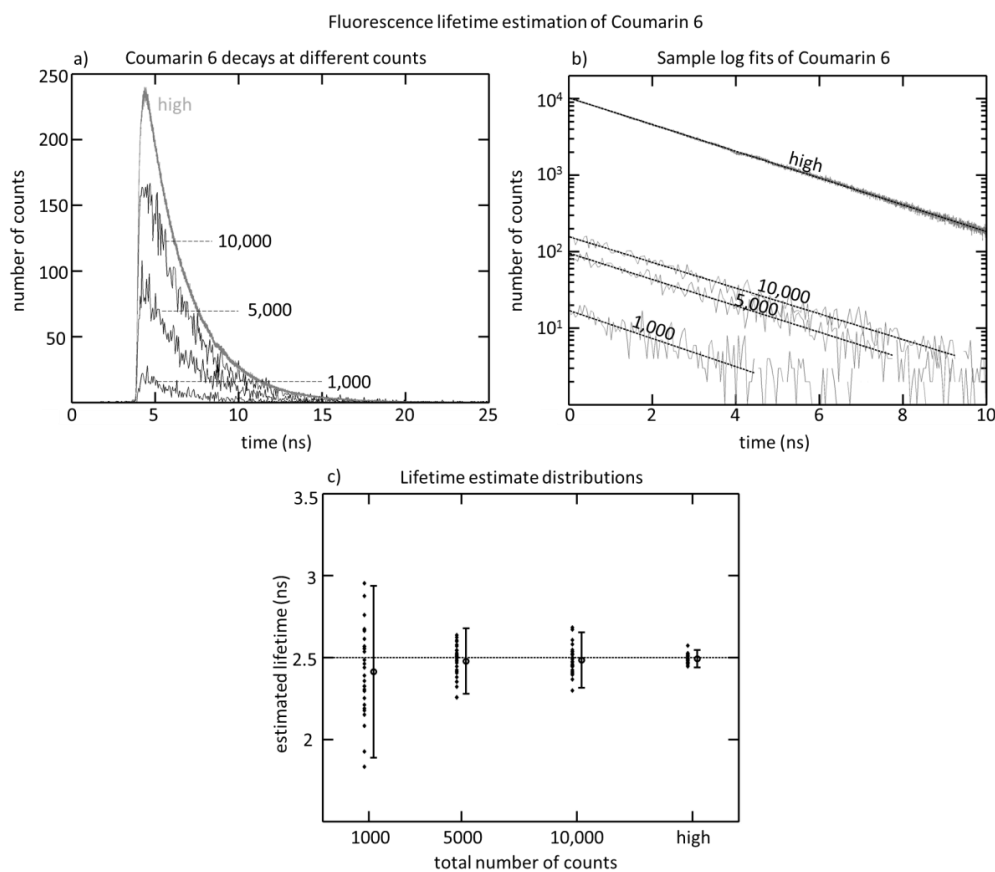


Figure 3. Fluorescence lifetime estimation of Coumarin 6. (a) TCSPC histograms for a SPAD after a range of different numbers of photon counts. The decay resulting from a “high” (>20,000,000) number of counts is scaled independently of the other three cases, and so does not correspond with the left axis; (b) logarithmic fits of TCSPC histograms under different count scenarios; and (c) results for lifetime estimation under each count scenario, as an ensemble of all SPADs in the array, with 95% confidence interval bounds.

4. Discussion

4.1. Noise Performance

The benefit of cooling the SPAD array to $-10\text{ }^{\circ}\text{C}$ is clear in the plots in Figure 2. At $25\text{ }^{\circ}\text{C}$, AP noise is insignificant compared to DCR noise. In Figure 2b, it can be seen that a weak 10 kcps fluorescence signal (along the horizontal axis) will already have 50% larger uncertainty than in the ideal shot noise case, and the uncertainty increases to twice the ideal value at a point 5 ns away from the decay peak. However, at $-10\text{ }^{\circ}\text{C}$ (Figure 2a), under the same conditions, these device-specific noise sources only increase the ideal shot noise by <5% and 10%, respectively. It is also clear that AP becomes the dominant source of added noise at higher collection rates.

The significance of these results depends greatly on how the histogram data is analyzed. It varies with which sections of the decay are important for the given lifetime estimation method. It could be that the shot noise is already at an insignificant level for the estimation, and so a doubling of this uncertainty is not very detrimental. In the case of HCS however, where you are likely to be starved for photon counts, a doubling of the uncertainty can, instead, be interpreted as requiring the scan rate to be reduced by a factor of four compared to the speed of an ideal TCSPC performance.

The plots in Figure 2 are calculated for a fluorescence lifetime of 5 ns. It is worth noting that shorter lifetime decays, as they are less spread out across the histogram, would be less affected by the device-specific noise sources.

4.2. Lifetime Estimation

The lifetime estimation experiment is not meant to demonstrate the precision with which a fluorescence lifetime can be found, since it depends on the lifetime extraction technique. Instead, it is designed to show the agreement between the lifetime of a standard fluorophore and all 32 channels of the SPAD array. The results show this to be true, as the estimated lifetime is more tightly restricted to the expected lifetime with an increasing number of counts.

It is also important to mention that no TCSPC channels tended to systematically over- or underestimate the fluorescence lifetime, and so the variability in lifetime measurement is a random spread. The TACs are found to be very linear and predictable.

4.3. Towards a 32×32 Array

The current challenge for the Milan team is to increase the custom-fabricated SPAD array size to 32×32 . This would be extremely attractive to HCS FLIM applications, achieving roughly the same multiplexing level as spinning disk confocal, but with the benefit of TCSPC collected behind each pixel.

As discussed briefly earlier, the task of scaling up the SPAD array is not straightforward. The primary issue is that the SPAD array chip needs to interface with the TAC array in a non-monolithic arrangement. This quickly becomes challenging when there are hundreds of SPADs. There is also the concern of bandwidth: if there are 1024 TACs that are each converting millions of counts to a timestamp each second, the data flow on the device quickly becomes unmanageable.

The proposed solution is to instead use 64 undedicated TACs to interface with the 1024 SPADs. A smart router setup has been designed whereby a detected photon count signal is routed to the next available TAC [44]. Each TAC has a maximum collection rate of 4 Mcps. This was not important before because the collection rate was ultimately limited by the 5% TCSPC limit for a single SPAD. In a smart router scenario where each TAC is not dedicated to a single SPAD, this limit no longer exists. It is, therefore, possible for 64 TACs to achieve a global collection rate of 256 Mcps.

For a uniform fluorescent sample, this would mean that each SPAD is limited to a collection rate of 250 kcps—significantly lower than the 2 Mcps afforded by the 5% TCSPC limit. Fortunately, images are typically more interesting than a uniform field. Due to the TAC smart routing, darker regions on a sample contribute less to the capacity of the TACs, and allow for brighter areas to exceed the 250 kcps average. For instance, if half of the foci are not collecting any signal, then the other half could have

a collection rate of 500 kcps. This capability would definitely depend on the target sample, but it is quite possible for a sparsely populated cell well to be unhindered by a dearth of TACs. In contrast, the Megaframe MF32 CMOS-based 32×32 SPAD array allows for a global collection rate of 500 Mcps, but each individual SPAD is limited to 500 kcps readout when using the entire array, consistent with the 500 kfps full-frame rate [23].

Data transfer rate is the other concern. As outlined as a requirement for HCS FLIM, the entire data transfer for a 512×512 image should be done in 1 s. For the case where 2^{14} time channels are used with a bit depth of 16 bits for each histogram, this amounts to a required data transfer rate of 69 Gbps—drastically higher than today's data connection standards. For our purposes, however, the number of time channels and bit depth are not sensible. If only 2^{10} time channels (25 ps per channel) and 10-bit-depth histograms (maximum 1024 counts per channel) are needed, the required data transfer rate is reduced to 2.7 Gbps—well within the 5 Gbps capabilities of a USB 3.0 connection.

5. Conclusions

The advent of the SPAD array brings great promise to many fields of research, and the advantages to HCS FLIM cannot be overstated. With the capability of multiplexing confocal and two-photon FLIM, SPAD array technology could finally make it feasible to apply FLIM-FRET protein-protein interaction studies to the realm of HCS. This would be a major advance for the drug discovery process.

There are a number of unique characteristics to SPADs that need to be taken into account when considering a multiplexed confocal setup. The PDE determines the SPAD's collection rate, while the DCR and afterpulsing determine the noise on the SPAD signal. The uniformity of each of these properties is also important. SPADs are prone to having sporadically high DCRs, for instance, which could mean that certain SPADs are collecting significantly lower quality signals. Optical crosstalk is another factor that could have significant effects on the multiplexed FLIM process. The impact of these factors on lifetime estimation is worth investigating further.

We also showed that the design of the 32×32 SPAD array should be able to perform FLIM imaging at a speed and precision suitable for HCS. Though the global collection rate is limited, the smart routing TAC setup should not significantly limit the collection rate for a typical live cell sample. The data transfer rate, when the TCSPC histogram data structure is reduced in size, should be well within the capabilities of USB 3.0 bandwidth.

Acknowledgments: This work was supported in part by the Ontario Centres of Excellence through a Market Readiness grant, the Natural Sciences and Engineering Research Council of Canada through an Idea to Innovation Grant and Industry Postgraduate PhD Scholarship (AT), and the Canadian Foundation of Innovation. QF held the Canada Research Chair in Biophotonics.

Author Contributions: A.T., P.P., I.R. and Q.F. conceived and designed the experiments and analyzed the data; A.T. and P.P. performed the experiments; NH contributed to the introduction; M.J.D. contributed to the discussion of the results; A.T. wrote the paper.

Conflicts of Interest: The authors declare no conflict of interest.

References

1. Bickle, M. The beautiful cell: High-content screening in drug discovery. *Anal. Bioanal. Chem.* **2010**, *398*, 219–226. [[CrossRef](#)] [[PubMed](#)]
2. Gaspari, F. An overview of cell phenotypes in HCS: Limitations and advantages. *Expert Opin. Drug Dis.* **2009**, *4*, 643–657. [[CrossRef](#)] [[PubMed](#)]
3. Sun, Y.; Day, R.N.; Periasamy, A. Investigating protein-protein interactions in living cells using fluorescence lifetime imaging microscopy. *Nat. Protoc.* **2011**, *6*, 1324–1340. [[CrossRef](#)] [[PubMed](#)]
4. Wallrabe, H.; Periasamy, A. Imaging protein molecules using FRET and FLIM microscopy. *Curr. Opin. Biotechnol.* **2005**, *16*, 19–27. [[CrossRef](#)] [[PubMed](#)]

5. Osterlund, E.J.; Liu, Q.; Andrews, D.W. The use of FLIM-FRET for the detection of mitochondria-associated protein interactions. In *Mitochondrial Medicine I: Probing Mitochondrial Function*; Weissig, V., Edeas, M., Eds.; Springer: New York, NY, USA, 2015; pp. 395–419.
6. Matthews, D.R.; Carlin, L.M.; Ofo, E.; Barber, P.R.; Vojnovic, B.; Irving, M.; Ng, T.; Ameer-Beg, S.M. Time-lapse FRET microscopy using fluorescence anisotropy. *J. Microsc.* **2010**, *237*, 51–62. [[CrossRef](#)] [[PubMed](#)]
7. Ishikawa-Ankerhold, H.C.; Ankerhold, R.; Drummen, G.P. Advanced fluorescence microscopy techniques—FRAP, FLIP, FLAP, FRET and FLIM. *Molecules* **2012**, *17*, 4047–4132. [[CrossRef](#)] [[PubMed](#)]
8. Lakowicz, J.R. Time-Domain Lifetime Measurements. In *Principles of Fluorescence Spectroscopy*; Springer: New York, NY, USA, 2006; pp. 97–155.
9. Becker, W. Fluorescence lifetime imaging—Techniques and applications. *J. Microsc.* **2012**, *247*, 119–136. [[CrossRef](#)] [[PubMed](#)]
10. Suhling, K.; French, P.M.W.; Phillips, D. Time-resolved fluorescence microscopy. *Photochem. Photobiol. Sci.* **2005**, *4*, 13–22. [[CrossRef](#)] [[PubMed](#)]
11. Arlt, J.; Tyndall, D.; Rae, B.R.; Li, D.D.-U.; Richardson, J.A.; Henderson, R.K. A study of pile-up in integrated time-correlated single photon counting systems. *Rev. Sci. Instrum.* **2013**, *84*, 103105. [[CrossRef](#)] [[PubMed](#)]
12. Palubiak, D.; El-Desouki, M.; Marinov, O.; Deen, M.J.; Fang, Q. High-speed, single-photon avalanche-photodiode imager for biomedical applications. *IEEE Sens. J.* **2011**, *11*, 2401–2412. [[CrossRef](#)]
13. Agronskaia, A.V.; Tertoolen, L.; Gerritsen, H.C. High frame rate fluorescence lifetime imaging. *J. Phys. D Appl. Phys.* **2003**, *36*, 1655–1662. [[CrossRef](#)]
14. Webb, S.E.D.; Gu, Y.; Lévêque-Fort, S.; Siegel, J.; Cole, M.J.; Dowling, K.; Jones, R.; French, P.M.W.; Neil, M.A.A.; Juskaitis, R.; et al. A wide-field time-domain fluorescence lifetime imaging microscope with optical sectioning. *Rev. Sci. Instrum.* **2002**, *73*, 1898–1907. [[CrossRef](#)]
15. Schneider, P.C.; Clegg, R.M. Rapid acquisition analysis and display of fluorescence lifetime-resolved images for real-time applications. *Rev. Sci. Instrum.* **1997**, *68*, 4107–4119. [[CrossRef](#)]
16. Philip, J.; Carlsson, K. Theoretical investigation of the signal-to-noise ratio in fluorescence lifetime imaging. *J. Opt. Soc. Am. A* **2003**, *20*, 368–379. [[CrossRef](#)]
17. Zhao, Q.; Young, I.T.; de Jong, J.G.S. Photon budget analysis for fluorescence lifetime imaging microscopy. *J. Biomed. Opt.* **2011**, *16*, 086007. [[CrossRef](#)] [[PubMed](#)]
18. Wachsmann-Hogiu, S.; Krakow, D.; Kirilova, V.; Cohn, D.H.; Bertolotto, C.; Acuna, D.; Fang, Q.; Krivorov, N.; Farkas, D.L. Multiphoton, confocal, and lifetime microscopy for molecular imaging in cartilage. *P. Soc. Photo-Opt. Inst.* **2005**, *5699*, 75–81.
19. An, W.F.; Tolliday, N. Cell-based assays for high-throughput screening. *Mol. Biotechnol.* **2010**, *45*, 180–186. [[CrossRef](#)] [[PubMed](#)]
20. Niclass, C.; Sergio, M.; Charbon, E. A single photon avalanche diode array fabricated in deep-submicron CMOS technology. In *Design, Automation, and Test in Europe*; Lauwereins, R., Madsen, J., Eds.; Springer: New York, NY, USA, 2008; pp. 401–413.
21. Lapington, J.S.; Ashton, T.J.R.; Ross, D.; Coneely, T. Progress towards a 256 channel multi-anode microchannel plate photomultiplier system with picosecond timing. *Nucl. Instrum. Meth. A* **2012**, *695*, 78–82. [[CrossRef](#)] [[PubMed](#)]
22. Becker, W.; Hirvonen, L.M.; Milnes, J.; Conneely, T.; Jagutzki, O.; Netz, H.; Smietana, S.; Suhling, K. A wide-field TCSPC FLIM system based on an MCP PMT with a delay-line anode. *Rev. Sci. Instrum.* **2016**, *87*, 093710. [[CrossRef](#)] [[PubMed](#)]
23. Krstajic, N.; Poland, S.; Levitt, J.; Walker, R.; Erdogan, A.; Ameer-Beg, S.; Henderson, R.K. 0.5 billion events per second time correlated single photon counting using CMOS SPAD arrays. *Opt. Lett.* **2015**, *40*, 4305–4308. [[CrossRef](#)] [[PubMed](#)]
24. Niclass, C.; Favi, C.; Kluter, T.; Gersbach, M.; Charbon, E. A 128 × 128 single-photon image sensor with column-level 10-bit time-to-digital converter array. *IEEE J. Solid-State Circ.* **2008**, *43*, 2977–2989. [[CrossRef](#)]
25. Villa, F.; Markovic, B.; Bellisai, S.; Bronzi, D.; Tosi, A.; Zappa, F.; Tisa, S.; Durini, D.; Weyers, S.; Paschen, U.; Brockherde, W. SPAD smart pixel for time-of-flight and time-correlated single-photon counting measurements. *IEEE Photonics J.* **2012**, *4*, 795–804. [[CrossRef](#)]
26. Cuccato, A.; Antonioli, S.; Crotti, M.; Labanca, I.; Gulinatti, A.; Rech, I.; Ghioni, M. Complete and compact 32-channel system for time-correlated single-photon counting measurements. *IEEE Photonics J.* **2013**, *5*, 6801514. [[CrossRef](#)]

27. Guerrieri, F.; Tisa, S.; Tosi, A.; Zappa, F. Two-dimensional SPAD imaging camera for photon counting. *IEEE Photonics J.* **2010**, *2*, 759–774. [[CrossRef](#)]
28. Kawakito, S.; Baek, G.; Li, Z.; Han, S.-M.; Seo, M.-W.; Yasutomi, K.; Kagawa, K. CMOS lock-in pixel image sensors with lateral electric field control for time-resolved imaging. In Proceedings of the International Image Sensor Workshop, Snowbird, UT, USA, 12–16 June 2013.
29. Chen, H.; Holst, G.; Gratto, E. Modulated CMOS camera for fluorescence lifetime microscopy. *Microsc. Res. Tech.* **2015**, *78*, 1075–1081. [[CrossRef](#)] [[PubMed](#)]
30. Hamamatsu Microchannel Plate Photomultiplier Tubes (MCP-PMT) R3809U-50 Series. Available online: https://www.hamamatsu.com/resources/pdf/etd/R3809U-50_TPMH1067E.pdf (accessed on 19 October 2016).
31. PicoQuant PDM Series Single Photon Avalanche Diodes. Available online: https://www.picoquant.com/images/uploads/downloads/pdm_series.pdf (accessed on 19 October 2016).
32. PicoQuant PMA Series Photomultiplier Detector Assembly. Available online: https://www.picoquant.com/images/uploads/downloads/pma_series.pdf (accessed on 19 October 2016).
33. Becker, W.; Su, B.; Holub, O.; Weisshart, K. FLIM and FCS detection in laser-scanning microscopes: Increased efficiency by GaAsP hybrid detectors. *Microsc. Res. Tech.* **2011**, *74*, 804–811. [[CrossRef](#)] [[PubMed](#)]
34. Tsikouras, A.; Ning, J.; Ng, S.; Berman, R.; Andrews, D.W.; Fang, Q. Streak camera crosstalk reduction using a multiple delay optical fiber bundle. *Opt. Lett.* **2012**, *37*, 250–252. [[CrossRef](#)] [[PubMed](#)]
35. Tsikouras, A.; Berman, R.; Andrews, D.W.; Fang, Q. High-speed multifocal array scanning using refractive window tilting. *Biomed. Opt. Express* **2015**, *6*, 3737–3747. [[CrossRef](#)] [[PubMed](#)]
36. Cuccato, A. Development of Electronic Systems for Single-Photon Avalanche Diode Arrays. Ph.D. Thesis, Politecnico di Milano, Milan, Italy, 2013.
37. Richardson, J.A.; Grant, L.A.; Henderson, R.K. A low dark count single photon avalanche diode structure compatible with standard nanometer scale CMOS technology. *IEEE Photonics Technol. Lett.* **2009**, *21*, 1020–1022. [[CrossRef](#)]
38. Palubiak, D.P.; Deen, M.J. CMOS SPADs: Design issues and research challenges for detectors, circuits and arrays. *IEEE J. Sel. Top. Quant.* **2014**, *20*, 600718. [[CrossRef](#)]
39. Palubiak, D.P.; Li, Z.; Deen, M.J. Afterpulsing characteristics of free-running and time-gated single-photon avalanche diodes in 130-nm CMOS. *IEEE T. Electron. Dev.* **2015**, *62*, 3727–3733. [[CrossRef](#)]
40. Akgun, U.; Ayan, A.S.; Aydin, G.; Duru, F.; Olson, J.; Onel, Y. Afterpulse timing and rate investigation of three different Hamamatsu photomultiplier tubes. *J. Instrum.* **2008**, *3*, T01001. [[CrossRef](#)]
41. Coates, P.B. The origin of afterpulses in photomultipliers. *J. Phys. D Appl. Phys.* **1973**, *6*, 1159–1166. [[CrossRef](#)]
42. Enderlein, J.; Gregor, I. Using fluorescence lifetime for discriminating detector afterpulsing in fluorescence correlation spectroscopy. *Rev. Sci. Instrum.* **2005**, *76*, 033102. [[CrossRef](#)]
43. Rech, I.; Ingargiola, A.; Spinelli, R.; Labanca, I.; Marangoni, S.; Ghioni, M.; Cova, S. Optical crosstalk in single photon avalanche diode arrays: A new complete model. *Opt. Express* **2008**, *16*, 8381–8393. [[CrossRef](#)] [[PubMed](#)]
44. Acconcia, G.; Crotti, M.; Rech, I.; Ghioni, M. High-performance timing electronics for single photon avalanche diode arrays. In Proceedings of the SPIE 9504: Photon Counting Applications, Prague, Czech Republic, 6 May 2015.

